AIP | Journal of Applied Physics

How does spallation microdamage nucleate in bulk amorphous alloys under shock loading?

X. Huang, Z. Ling, H. S. Zhang, J. Ma, and L. H. Dai

Citation: J. Appl. Phys. **110**, 103519 (2011); doi: 10.1063/1.3663332
View online: http://dx.doi.org/10.1063/1.3663332
View Table of Contents: http://jap.aip.org/resource/1/JAPIAU/v110/i10
Published by the American Institute of Physics.

How does spallation microdamage nucleate in bulk amorphous alloys under shock loading?

X. Huang,[1] Z. Ling,[1] H. S. Zhang,[1] J. Ma,[2,3] and L. H. Dai[1,a)]
[1]*State Key Laboratory of Nonlinear Mechanics, Institute of Mechanics, Chinese Academy of Sciences, Beijing 100190, China*
[2]*School of Materials Science and Engineering, Nanyang Technological University, Singapore 639798, Singapore*
[3]*Temasek Laboratories, Nanyang Technological University, Singapore 637553, Singapore*

(Received 3 June 2011; accepted 22 October 2011; published online 29 November 2011)

Specially designed plate-impact experiments have been conducted on a Zr-based amorphous alloy using a single-stage light gas gun. To understand the microdamage nucleation process in the material, the samples are subjected to dynamic tensile loadings of identical amplitude ($\sim$3.18 GPa) but with different durations (83–201 ns). A cellular pattern with an equiaxed shape is observed on the spallation surface, which shows that spallation in the tested amorphous alloy is a typical ductile fracture and that microvoids have been nucleated during the process. Based on the observed fracture morphologies of the spallation surface and free-volume theory, we propose a microvoid nucleation model of bulk amorphous alloys. It is found that nucleation of microvoids at the early stage of spallation in amorphous alloys results from diffusion and coalescence of free volume, and that high mean tensile stress plays a dominant role in microvoid nucleation. © *2011 American Institute of Physics*. [doi:10.1063/1.3663332]

I. INTRODUCTION

Spallation is a typical dynamic fracture process of solids under impulsive tensile loadings. It has been studied by researchers for several decades, and the process of nucleation, growth, and coalescence of microdamage is known to be the principle mechanism.[1] Spallation is recognized as a rate-dependent and microstructure-dependent microdamage evolution process which results in catastrophic failure of solids.[2,3] Considerable work has been done on spallation in conventional polycrystalline alloys. It has revealed that in ductile fracture, spallation occurs via nucleation, growth, and coalescence of microvoids,[4,5] while in brittle fracture, spallation occurs via nucleation, growth, and coalescence of microcracks.[6,7]

Although the mechanism of spallation in conventional polycrystalline alloys is understood, the mechanism of spallation in bulk amorphous alloys is unclear. As a relatively young class of alloy materials, bulk amorphous alloys[8–10] have many excellent physical and mechanical properties such as high strength and hardness due to their unique microstructure. Quite differently from their crystalline alloy counterparts, amorphous alloys have disordered atomic structure that is induced by fast cooling from the liquid to solid states.[11–15] Also, no traditional defects can be found in polycrystalline materials such as vacancies, dislocations, grain boundaries, and so on. Instead, free volume[16,17] is thought to be the most common defect, and shear transformation zones (STZs)[18–20] and tension transformation zones (TTZs)[21–24] are the fundamental unit-processes of collective atomic motion in amorphous alloys. Since the damage evolution of spallation is known to be closely related to microstructures and intrinsic defects of materials, the nucleation mechanism of spallation damage in amorphous alloys should have some differences from that of polycrystalline alloys.

Recently, several researchers have reported dynamic behavior of amorphous alloys,[24–32] and work has been carried out to investigate spallation strength, Hugoniot elastic limit (HEL), the microscopic characteristics of spalled surfaces, and—as part of this—the development of spall in amorphous materials via plate-impact tests. Zhuang *et al.*[25] examined the shock response of a Zr-based amorphous alloy (Vit 1) and its composites. By using the velocity interferometer system for any reflector (VISAR) to obtain the rear surface velocity history of the samples, they determined the spall strength of Vit 1 to be 2.35 GPa. It is thought that spallation in Vit 1 is induced by shear localization, while that in β-Vit is due to debonding of the β-phase boundary from the matrix. Gupta and his coworkers[24,26] studied the dynamic tensile response of another Zr-based amorphous alloy ($Zr_{56.7}Cu_{15.3}Ni1_{2.5}Nb_{5.0}Al_{10.0}Y_{0.5}$) under plate-impact loading. Based on the free-surface velocity history measured by VISAR, they determined the onset stress for spallation to be 3.8 GPa and the HEL to be about 7 GPa. The tested samples exhibited a change from ductile to brittle fracture as the impact stress increased. According to the fracture morphology on the spallation surface of the samples, it was shown that the tested samples exhibit both ductile behavior (for microscopic voids and dimples found on fracture surface) and brittle behavior (for macroscopic cracks). Fracture mechanisms at different levels were proposed, and it was revealed that high tensile loading rate, high mean tensile stress, and free volume content play key roles in the spallation process. Yuan *et al.*[27,28] investigated influences

a)Author to whom correspondence should be addressed. Electronic mail: lhdai@lnm.imech.ac.cn.

TABLE I. Mechanical properties of Vit 1.

Materials	ρ (kg/m^3)	E (Gpa)	μ (Gpa)	v	$c_{L\ (m/s)}$	$c_{t\ (m/s)}$
Vit 1	6125	96	35.3	0.36	5185	2464

of impact stress and shear strain on the spallation strength of Vit 1. They found that under normal shock-compression loading, the spall strength of Vit 1 decreases as the impact stress increases. But under combined compression-and-shear loading, the spall strength showed an unusual trend under the effects of shear strain. Thadhani and co-workers[29–31] studied the dynamic compression response, phase stability, and Hugoniot equation of state (EOS) of the Zr-based amorphous alloy $Zr_{57}Nb_5Cu_{15.4}Ni_{12.6}Al_{10}$. In their anvil-on-rod experiments, they found several fracture planes perpendicular to the loading axis in an unsleeved specimen, which appeared to indicate multiple spallation. Close observation of these fracture planes found dimple structures, and it was shown that brittle amorphous alloys have some ductility. These works provide important information for understanding spallation in amorphous alloys. However, some basic questions about nucleation of spallation have not been answered. As the microstructure of amorphous alloys is quite different from conventional polycrystalline alloys, what is the microdamage of spallation in amorphous alloys, microvoids or microcracks? And what is the microdamage nucleation mechanism?

To this end, we investigate spallation in a Zr-based amorphous alloy under dynamic tensile loading. We conduct plate-impact experiments using a loading apparatus specially designed to achieve dynamic tensile loading of identical amplitude but with different stress durations. All the recovered samples are examined by a scanning electron microscope (SEM) to characterize the spallation surface morphologies and fracture features. Based on the fracture morphologies of the spallation surface and free-volume theory, we propose a spallation damage nucleation model in bulk amorphous alloys.

II. EXPERIMENTAL PROCEDURE

The material we used was a Zr-based amorphous alloy with the nominal composition $Zr_{41.2}Ti_{13.8}Cu_{12.5}Ni_{10}Be_{22.5}$ (Vit 1). Conventional x-ray diffraction verified that all the samples were fully amorphous before the spallation experiments. Table I presents the mechanical properties of Vit 1 extracted from other literatures,[27,33,34] where ρ is the density, E the elastic modulus, G the shear modulus, ν the Possion ratio, c_L the longitudinal wave speed, and c_t the shear wave speed.

The plate-impact experiments[2,35,36] were performed with a 101 mm single-stage light gas gun. The flyer material used was H62 brass, which is similar to C28000 brass (e.g., 62% Cu and 38% Zn). We used a multi-stress pulse technique to study the evolution of microdamage.[37] With this technique, several samples were impacted by several flyers with different thickness in one shot, so that the impact stress kept the same amplitude but had different durations. Then, different evolution stages of the microdamage were frozen in the tested samples. Figure 1 displays the schematic of the plate-impact apparatus, where Figs. 1(a) and 1(b) show specially designed flyers and targets, respectively. As is shown in Fig. 1, four flyers with different thickness were embedded in the holes of one impactor, and four samples were placed at the corresponding positions of one target. To keep the complex samples flat and parallel, we first put the target plate with 4 holes on a surface plate (600 mm $\times$ 400 mm) which was extremely flat with surface roughness (Ra) of 7 μm. Then, the carefully lapped and polished samples were imbedded in the holes. Because all samples were in touch with the surface plate, they were kept parallel. After that, the samples were bonded to the holes with epoxide resin. The impact surface of the target was carefully lapped and polished before each test. Effort must also be made to avoid the influence of projectile rotation, so the maximal rotation angle should be predicted before the spallation experiments. According to our calibration experiments, the projectile rotation angle is always less than $\sim 1^\circ$. The diameter of the flyers, which is bigger than that of the samples, was designed for the maximal rotation angle, so that each flyer could cover the corresponding sample during the tests. Each of our flyers was 22 mm in diameter, while the samples were 8 mm. Because the flyers were much bigger than the samples, it might be expected that the projectile rotation would have little influence on the results. The impact velocity was determined by recording the times at which two isolated charged pins, set at different spacings from the target plate, were shorted to ground. With the distance between pins and the time intervals, we obtained the plate impact velocity.

Table II lists the experimental details, where h is the flyer thickness, δ the target thickness, Δt the stress duration,

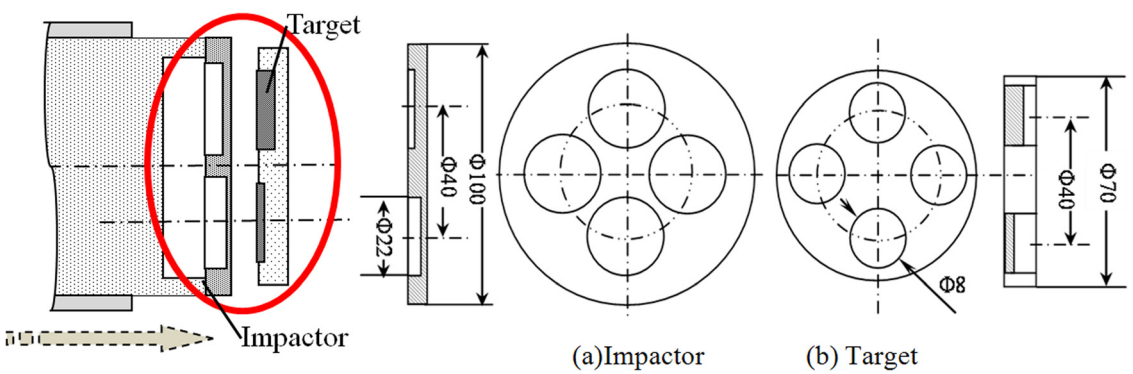

FIG. 1. (Color online) Schematic of the plate-impact apparatus. (a) Impactor. (b) Target.

TABLE II. Summary of plate-impact experiments (impact speed = 200 m/s).

Sample	Flyer thickness h(mm)	Target thickness δ(mm)	Designed duration Δt(ns)	$\sigma_T = 3.18$ Gpa
1–1	0.585	1.04	201	Detached spallation
1–2	0.45	0.09	174	Cracks
1–3	0.335	0.64	123	Cracks
1–4	0.135	0.43	83	No cracks
2–1	0.585	1.03	199	Detached spallation
2–2	0.04	0.85	164	Cracks
2–3	0.335	0.63	122	N.A.
2–4	0.135	0.44	85	No cracks

and σ_T the impact stress amplitude. Each sample was machined to an 8-mm diameter disk while the flyers were machined to a 22-mm disk. All the flyers and samples were lapped on both sides to a desired thickness. We designed the stress to have durations of a few tenths of a microsecond, 10^1–10^2 ns, less than 200 ns. Two plate-impact experiments were performed at impact speed of 200 m/s.

III. RESULTS AND DISCUSSION

Close-up observations with a high resolution scanning electronic microscopy (HRSEM) (FEI-Sirion NC HRSEM with 1.5 nm resolution) were performed to recovered samples. For the spalled samples, fractography of spall surfaces was examined. And for the samples with shorter durations, their cross-sections were checked to make sure if spallation microdamage had occurred in the samples. As the samples are centre-symmetrical disks subjected to centre-symmetrical loading and the radial release wave is initiated from lateral boundaries of the samples, resultant spallation as well as spalling microdamage shall occur in a central region,[1] or spallation region, of the disk-like samples. The close-up observations to the tested samples show that no voids or cracks are found in regions beyond the spallation region of each sample.

Typical micrographs of the recovered samples under tensile loading of identical amplitude of 3.18 GPa but different durations are presented in Fig. 2. Figures 2(a) and 2(b) exhibit half part of the spallation region in cross sections of samples with shorter durations, 83 and 123 ns, respectively. An insert to Fig. 2 is a schematic of disk-like samples. The spallation region (dark shaded) in the examined cross-section (light shaded) is along the radial direction, normal to loading directions (arrows' indicating), and far away from the lateral boundary of the disk-like sample. The marked square is the exact location of the regions illustrated in Figs. 2(a) and 2(b). Figure 2(c) shows the free surface of one spalled sample with the duration of 201 ns. As is illustrated in Fig. 2, the recovered samples show spallation damage at different levels. For the sample with the duration of 83 ns, no cracks were observed in the cross section (Fig. 2(a)). But as the duration increased to 123 ns in Fig. 2(b), a main crack, about 200–250 μm in length was found propagating from left (the sample's center) to right (towards the sample's lateral boundary) and along a wavy route. However, only part of the crack is perpendicular to the loading axis. Figure 2(c) shows the free surface of the sample with the duration of 201 ns. A crater with a diameter of 1–2 mm and depth of 300–400 nm can be seen at the center of the free surface, which suggests that a detached spallation has occurred in this sample. The damage at different levels shown in Fig. 2 indicates that spallation in amorphous alloys is a damage evolution process as the stress duration increases under the same stress level.

The crater on the free surface of a recovered sample ($\sigma_T = 3.18$ GPa and $\Delta t = 201$ ns) was examined carefully to get more information on spallation. An overview of the crater is presented in Fig. 3. It should be noted that as detached spallation occurs, spallation fragments break away from the free surface forming the observed crater. Figure 3(a) shows the electron micrographs of the crater, and Fig. 3(b) is a schematic cross section of the recovered sample. As presented in Fig. 3, the bottom of crater is almost perpendicular to the loading axis and is located in the sample. However, at the edge of the crater, the fracture plane has deviated from the usual spallation plane. It is believed that spallation occurs

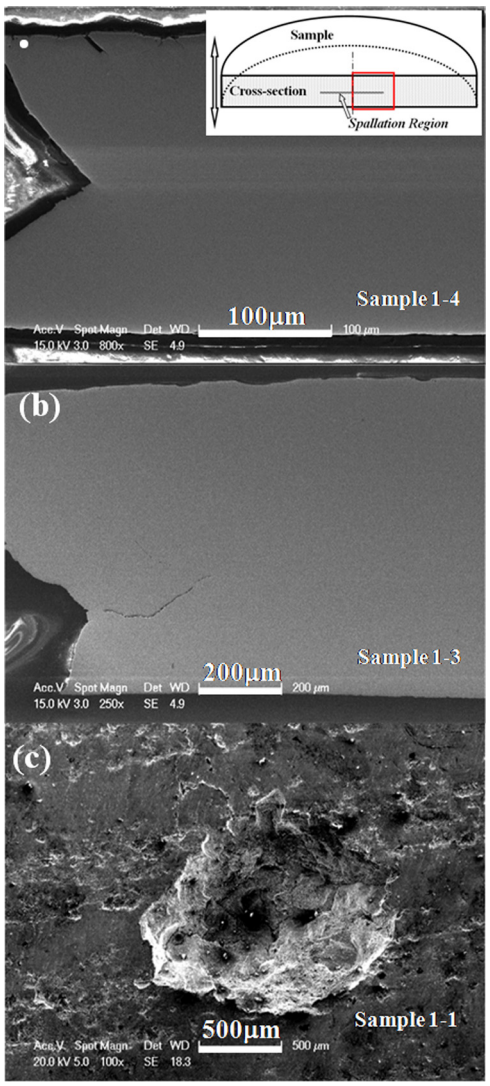

FIG. 2. (Color online) Close-up observations of Zr-based amorphous alloy samples with different durations: the central part of cross-sections of (a) sample 1–4 (83 ns) and (b) sample 1–3 (123 ns); (c) the free surface of sample 1–1(201 ns).

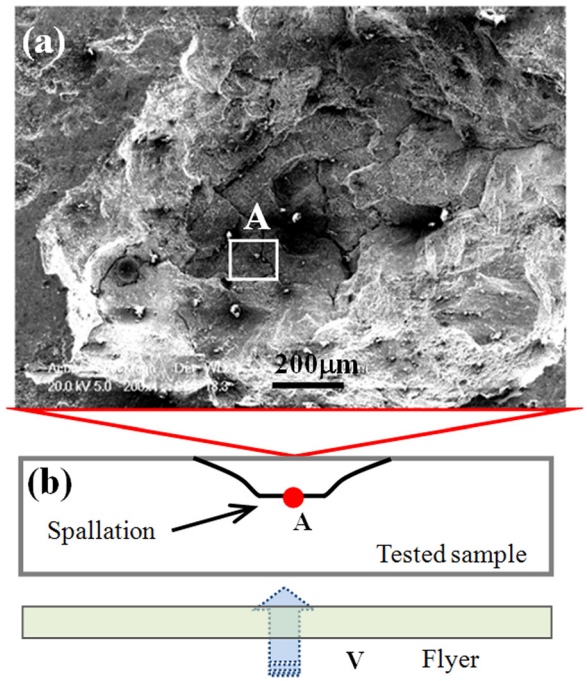

FIG. 3. (Color online) Crater on the free surface of the tested sample (3.18 GPa, 201 ns). (a) SEM micrograph, where region A is located at the bottom of the crater. (b) Schematic cross section of the crater.

first at the bottom and then propagates to the edge of the crater. The bottom is part of the spall surface where the material is under hydro-tensile stress and subjected to a peak tensile stress. Region A is just located at the bottom of the crater, so details in region A can offer important information on spallation in the recovered sample.

Figure 4 shows the characteristics of the fracture surface in region A. A SEM micrograph of region A is given in Fig. 4(a), where a cellular pattern is observed. Details of the squared zone in Fig. 4(a) (region B) are exhibited in Fig. 4(b). The cellular pattern consists of voids or dimples in approximately equiaxed shape, with a diameter less than 10 μm. In particular, the cellular pattern appears to be built by microvoid stacking, so that under higher magnifications, this dimple structure is a porous structure with interconnected voids. Meanwhile, some small white particles, less than 100 nm, are found in dimple cell walls.

The experimental results and observations uncover some crucial features of spallation behavior in amorphous alloys. First, it is revealed that spallation within the materials is a kind of ductile fracture at the microscopic level, which is also recently reported by Escobedo and Gupta.[24] A little difference is that the spallation surface in our experiments seems to exhibit more ductility than that observed by Escobedo and Gupta. As is indicated by Turneaure *et al.*,[26] spallation in amorphous alloys exhibits a change from ductile to brittle fracture as the impact stress increases. This can be explained by the lower amplitude used in our tests. Second, the spallation damages in amorphous alloys are microvoids, especially at the microscopic level. Microvoids have also been observed in other spallation experiments.[24,25] However, there is still some difference. The microvoids observed by Zhuang *et al.*[25] were within the zip-shaped cracks thought to be formed by nucleation, growth, and coalescence of microvoids in the shear bands. The microvoids observed by Escobedo and Gupta[24] were in the plane that was parallel to the spall plane, and river-like patterns were also observed. The microvoids in our study were also in the plane parallel to the spall plane, but were not as coarse as those observed by Escobedo and Gupta.[24] We find no river pattern related to shear stresses. Third, the high mean tensile stress seems to play a more dominant role than shear stress. As is shown in Figs. 3 and 4, the spallation plane is perpendicular to the loading axis, and the cellular pattern has an equiaxed shape and lacks a certain orientation. This suggests that no shear-induced slip occurs during spallation, and mean tensile stress plays a dominant role. Furthermore, details about spallation damage (microvoids) can be obtained. Because the void size at the final stage of spallation damage evolution is several μm, the critical nucleation size should be much smaller than that scale. The time needed for nucleation is much shorter because the time needed for detached spallation is about 200 ns.

However, other questions have not been answered. How do these microvoids nucleate during spallation in amorphous alloys? And how does the high mean tensile stress act during void nucleation? To understand these questions, we propose a nucleation model based on free-volume theory in amorphous alloys in Sec. IV.

IV. PROPOSED NUCLEATION MODEL

Nucleation is defined as the creation of voids or cracks that are large enough to grow under applied stress. For spallation in conventional polycrystalline materials, void nucleation is usually interpreted by stress/temperature-driven models[1] because the hydro-tensile stress is more dominant than the shear stress. According to stress/temperature-driven models,[38–40] vacancies can diffuse through the matrix and in

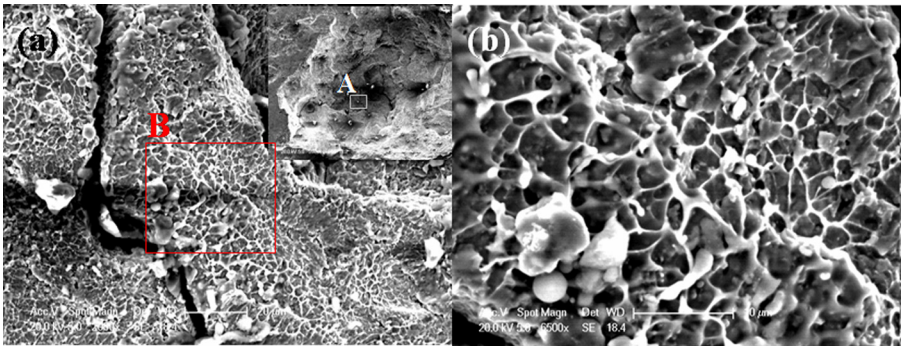

FIG. 4. (Color online) (a) Cellular pattern in region A. (b) Details of cellular pattern with equiaxed shape in region B.

grain boundaries by thermal activation. Under the right conditions, vacancy clusters (or voids) can form and grow by the diffusive motion of vacancies toward them. Once a critical size is reached, they can grow rapidly under tensile loading. Then, the voids are considered to be nucleated.

These stress/temperature-driven models cannot be directly used to explain the mechanism of void nucleation in amorphous alloys. The microstructures of amorphous alloys are quite different compared with conventional polycrystalline materials. There are no grains or grain boundaries in amorphous alloys. Also, free volume is thought to be the most common defect in amorphous alloys, whereas vacancies, inclusions, and dislocations are the most common in conventional polycrystalline materials. However, there are still some similarities. First, though free volume is different from vacancies, both can be regarded as voids on the atomic scale, which are the basis of nucleation. Second, the diffusion of atoms in amorphous alloys is similar to that in polycrystalline materials, both of which can be interpreted in terms of a single atomic jump mechanism.[41] So the diffusion mechanism of free volume is similar to that of vacancies. Thus, we believe that there must be some similarities between void nucleation in amorphous alloys and void nucleation in polycrystalline materials.

According to the results of our experiments, the spallation in Vit 1 is controlled by nucleation and evolution of many microvoids. Here, we propose a void nucleation model of amorphous alloys developed from traditional stress-temperature-driven models widely used in polycrystalline materials.[1,38–40] We also consider free-volume theory[16,42,43] to understand and characterize microvoid nucleation in bulk amorphous alloys.

In our model, the process of void nucleation can be divided into three stages: First, the frozen free volume is activated by applied tensile stress; second, free volume diffuses in the material and causes a net diffusional coalescence; and third, a void that is larger than a critical size forms and grows under tensile loading. At this stage, we consider the void to be nucleated.

A. Activation of free volume

The initial free volume is thought to be frozen in amorphous alloys because of the small atomic mobility at ambient temperature.[16,44] But as a bulk amorphous alloy is subjected to dynamic tensile loading, free volume can no longer remain stable. The size and location of free volume can continuously change. At this stage, we consider the free volume to be activated. Under shock loading, there are three effects that activate the frozen free volume.

1. Increase of free volume content

The first effect of applied loading on amorphous alloys is the increase of the initial free volume in the system for the effect of mean tensile stress.[34,45] During spallation, the material is subjected to dynamic tensile stress of several GPa or higher. As the mean tensile stress causes volume dilation, the average free volume increases. According to free-volume theory,[16,42,43] for an atom to jump, it must have a free volume large enough to accommodate its hard-sphere volume v^*. For the increase of average free volume, there is a higher probability for an atom to have a free volume larger than v^*. Then, the friction of the potential jump sites increases.

When a bulk amorphous alloy is subjected to a dynamic tensile loading, the bulk strain in our uniaxial strain condition is

$$\Delta = \varepsilon_T = \frac{\sigma_T}{E_L} = \frac{\sigma_T(1+\nu)(1-2\nu)}{(1-\nu)E}, \tag{1}$$

where ε_T is the axial strain, σ_T the applied tensile stress, E the Young's modulus, E_L the constrained modulus, and ν the Poisson's ratio.

Assuming that the hard sphere atomic volume v^* is held constant and all of the dilation is attributed to a change in free volume,[34] the average free volume, v_{f1}, under tensile loading can be written as

$$v_{f1} = (v^* + v_{f0})(1+\varepsilon_T) - v^*, \tag{2}$$

where v_{f0} is the original average free volume.

Thus, according to free-volume theory,[16,42,43] the probability of finding an atom with a free volume between v and $v+dv$ under tensile loading is

$$p_1(v)dv = \frac{\gamma}{v_{f1}}\exp\left(\frac{-\gamma v}{v_{f1}}\right)dv, \tag{3}$$

where γ is a geometric factor between 1/2 and 1. In fact, as extra free volume is created by mean tensile stress, the statistical distribution of free volume cannot become $p_1(v)$ immediately, and redistribution time is needed. In this model, we directly use $p_1(v)$ for simplicity. Then, the total probability that an atom is at a potential jump site is

$$\int_{v^*}^{\infty}\frac{\gamma}{v_{f1}}\exp\left(-\frac{\gamma v}{v_{f1}}\right)dv = \exp\left(-\frac{\gamma v^*}{v_{f0}+(v^*+v_{f0})\varepsilon_T}\right). \tag{4}$$

2. Decrease of activation barrier

The second effect of applied loading is the decrease of the activation barrier that an atom must overcome when it jumps from one site to another. The average spacing between atoms becomes larger with volume dilation of the material, which decreases the activation barrier. In fact, the tensile loading can be divided into mean and deviatoric stresses, and both of them contribute to volume dilation in amorphous alloys. However, compared with the mean tensile stress, the shear-induced dilation in amorphous alloys is a secondary effect.[46,47] The volume dilation caused by deviatoric stress is significantly smaller than that caused by mean tensile stress, so we only consider mean tensile stress in this model.

The influence of mean tensile stress on the activation barrier is interpreted as the mechanism shown in Fig. 5. In order to make an atom jump, some activation energy must be

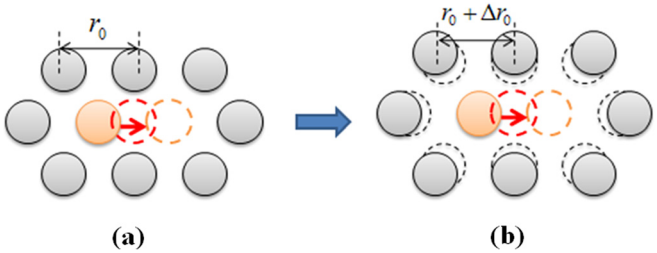

FIG. 5. (Color online) Influence of mean tensile stress on activation barrier.

supplied. The activation barrier is determined by the atom's nearest-neighbor environment. It changes as the nearest-neighbor environment is changed by the external forces. And the activation barrier can be expressed by the potentials between the jumping atom and its neighboring atoms, similarly to the theory used in molecular dynamics simulations.[48,49] If the average atomic spacing of the intact material is denoted as $\bar{r}$ and the interaction between atoms is described by potential function $\phi(r)$, where r is the spacing between two atoms, the activation barrier can be written as

$$\Delta G_m(\bar{r}) = \sum_{i=1}^{n} \phi_i(A_i\bar{r}) - \sum_{j=1}^{n} \phi_j(B_j\bar{r}), \tag{5}$$

where the first term of the right side of Eq. (5) is the maximum potential energy of the single-atom jump process, n the number of nearest atoms that influence the jump, $A_i\bar{r}$ the distance between the jumping atom and nearest atom (i) and A_i a coefficient related to the nearest-neighbor environment. A_i is assumed to be constant. The second term of the right side of Eq. (5) is the initial potential energy before the jump, which is similar in form to the first term.

As the material is subjected to tensile loading, the average atomic spacing increases from r_0 to $r_0 + \Delta r_0$. When the volume dilation is not very large, Δr_0 is much smaller than r_0. As a first approximation, the new activation barrier can be written as

$$\Delta G_m(r_0 + \Delta r_0) = \Delta G_m(r_0) + \left.\frac{d\Delta G_m(\bar{r})}{d\bar{r}}\right|_{\bar{r}=r_0} \Delta r_0. \tag{6}$$

Because Δr_0 is proportional to the bulk strain Δ and Δ is proportional to the mean tensile stress σ_m, we can obtain

$$\Delta G_m(r_0 + \Delta r_0) - \Delta G_m(r_0) = -c_0\sigma_m, \tag{7}$$

where c_0 is a coefficient related to the influence of the mean tensile stress on the activation barrier. It is difficult to determine the value of c_0, but we can estimate it using the diffusion theory of crystalline solids.[50]

For a defect-mediated diffusion process in polycrystalline materials, the diffusion coefficient D can be written as

$$D = d^2 v_0 \exp\left(\frac{-\Delta G_v}{kT}\right) \exp\left(\frac{-G_m}{kT}\right), \tag{8}$$

where d is the average jump length of an atom, v_0 the Debye frequency, ΔG_v the energy of forming a vacancy, and ΔG_m the activation barrier.

With the aid of the thermodynamic relation $(\partial G/\partial p)_T = V$, one can derive the pressure dependence and the activation volume of diffusion using

$$\left[\frac{\partial \ln(D/(d^2 v_0))}{\partial p}\right]_T = \frac{-1}{kT} V_{act} = \frac{-1}{kT}(V_v + V_m), \tag{9}$$

where V_{act} is an activation volume composed of a formation term V_v and a migration term V_m. V_m can also be used to estimate the value of c_0. Because the migration volume V_m of many amorphous alloys has been obtained from diffusion experiments and numerical simulations,[44] c_0 can be calculated.

3. Temperature rise

It should be noted that the material is subjected to an initial compressive stress before dynamic tensile loading starts. During compression, part of the stress wave energy is transferred to heat energy, which raises the temperature of the material.[2] As the temperature rises, atoms have a higher chance of getting enough energy from thermal fluctuations to overcome the activation barrier. This is the third effect of applied loading on amorphous alloys. But if the compressive stress is not very high, especially below the HEL, the compression and release of the material is elastic. The temperature rise is not expected to be very high and can be ignored. Because the HEL of Vit 1 is about 6.15 GPa,[27] much higher than the applied loading (3.18 GPa) in our work, temperature rise is not considered for simplicity in this model.

B. Diffusion of free volume

As the free volume is activated, it diffuses and rearranges in the material. Thus, the size and location of free volume changes continuously. We note that free-volume diffusion induces two opposing processes: (1) free volumes coalesce with each other to form larger ones (or free-volume clusters); and (2) large free volumes shrink by dividing into smaller ones. If there is no void nucleation, these two processes will balance each other. All the free volume, including the part newly added by volume dilation, is randomly distributed so that the free energy of the amorphous alloy system is a minimum.

However, there is a critical size for free volumes because of the external tensile stress. Once a free volume becomes larger than the critical size, it can grow under tensile loading and does not shrink any more. At this stage, a void is considered to be nucleated. Thus, similar to void nucleation in conventional polycrystalline materials,[1] void nucleation in amorphous alloy can be interpreted as the appearance of voids large enough to grow under applied tensile loading.

The critical size can be obtained by using the maximum in the free-energy function.[39,40] We consider the void nucleation at constant pressure and temperature in amorphous alloys. The formation of one void nucleus contributes to the change in free energy of the system through the following factors: (1) the work done by the system on its surroundings, (2) the energy needed to form the new surface area of the void, and (3) the change in stored elastic energy in the system. Usually, factor (3) can be neglected because factor (1),

which is of order σ_T, is much larger than factor (3), which is of order σ_T^2/E. Therefore, the critical condition is: when the work done on an element containing a virtually growing void is more than enough to create the new void surface area, the void can be considered "nucleated." That is,

$$\sigma_T dv > \gamma_m da, \tag{10}$$

where dv is an increase in void volume, γ_m the surface energy of amorphous alloys, and da the increase in void surface area. Below the critical size, the void can grow only by free volume diffusion because the external work is not sufficient. If we consider a spherical void, $dv = 4\pi r^2 dr$ and $da = 8\pi r dr$. Thus, the critical radius can be obtained from the formula

$$r_c = 2\gamma_m/\sigma_T. \tag{11}$$

It is obvious that the two opposing processes during the free-volume diffusion cannot keep balanced under tensile loading. Because a free volume larger than the critical size does not shrink any more, the shrinking process is weaker than the coalescence process. Thus, there is a net coalescence during the diffusion of free volume.

C. Nucleation rate

Figure 6 shows the schematic of void nucleation. We consider a free volume with a size between $v_c - v^*$ and v_c, where v_c is the critical volume obtained from the critical radius r_c. This free volume can also be called the subcritical nuclei. If an atom jumps from the inner surface into the outer environment, it means a volume of v^* is added to the subcritical nucleus. Then, the subcritical nucleus becomes larger than the critical size, and a void is nucleated. The nucleation rate per unit volume can be derived from the number of subcritical nuclei per unit volume, ρ_c, and from the time-dependent probability p_i of one atom jumping from the inner surface into the outer environment.

Under tensile loading, the number of subcritical nuclei per unit volume is

$$\begin{aligned}\rho_c &= n_0 \int_{v_c - v^*}^{v_c} \frac{\gamma}{v_{f1}} \exp\left(-\frac{\gamma v}{v_{f1}}\right) dv \\ &= n_0 \left[\exp\left(\frac{\gamma v^*}{v_{f1}}\right) - 1\right] \exp\left(-\frac{\gamma v_c}{v_{f1}}\right),\end{aligned} \tag{12}$$

where n_0 is number of atoms per unit volume.

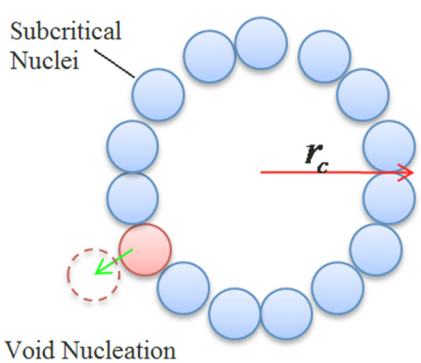

FIG. 6. (Color online) Schematic of void nucleation.

p_i can be derived from the jumping frequency of an atom and the number of atoms on the inner surface of a subcritical nucleus.

The jumping frequency of an atom is

$$v_0 \exp\left(-\frac{\Delta G'_m}{kT}\right) \exp\left(-\frac{\gamma v^*}{v_{f1}}\right), \tag{13}$$

where $\Delta G'_m$ is the activation barrier under tensile loading, v_0 the Debye frequency, and k Boltzmann's constant.

From Eq. (7), the activation barrier under tensile loading $\Delta G'_m$ (which is $\Delta G_m(r_0 + \Delta r_0)$ in Eq. (7)) is

$$\Delta G'_m = \Delta G_m - V_m \frac{(1+\nu)\sigma_T}{3(1-\nu)}, \tag{14}$$

where V_m is the migration volume used to evaluate the value of c_0, σ_T the applied tensile stress under uniaxial strain condition, and ν the Poisson's ratio.

The number of atoms on the inner surface of a subcritical nucleus is

$$\frac{4\pi r_c^2}{d^2} \approx \frac{4\pi r_c^2}{v^{*2/3}}. \tag{15}$$

Therefore, p_i can be derived using

$$p_i = \frac{4\pi r_c^2}{v^{*2/3}} v_0 \exp\left(-\frac{\Delta G_m - V_m \sigma_T (1+\nu)/(3-3\nu)}{kT} - \frac{\gamma v^*}{v_{f1}}\right). \tag{16}$$

Then, the nucleation rate per unit volume is

$$\begin{aligned}\dot{N} = n_0 &\left[\exp\left(\frac{\gamma v^*}{v_{f1}}\right) - 1\right] \exp\left(-\frac{\gamma v_c}{v_{f1}}\right) \frac{4\pi r_c^2}{v^{*2/3}} v_0 \\ &\times \exp\left(-\frac{\Delta G_m - V_m \sigma_T (1+\nu)/(3-3\nu)}{kT} - \frac{\gamma v^*}{v_{f1}}\right).\end{aligned} \tag{17}$$

Because $\exp(\gamma v^*/v_{f1}) - 1 \approx \exp(\gamma v^*/v_{f1})$, v^* is of order $10 v_{f0}$, γ lies between 1/2 and 1, $v_{f1} = v_{f0} + (v^* + v_{f0})\varepsilon_T \approx v_{f0}$ (with ε_T of order 0.01) and $r_c = 2\gamma_m/\sigma_T$, Eq. (17) can be written as

$$\dot{N} = \frac{A}{\sigma_T^2} \exp\left(B\sigma_T - \frac{C}{\sigma_T^3}\right), \tag{18}$$

where

$A = n_0 \frac{16\pi\gamma_m^2}{v^{*2/3}} v_0 \exp(-\frac{\Delta G_m}{kT})$ is a material constant at a certain temperature,

$B = \frac{V_m}{kT} \frac{1+\nu}{3(1-\nu)}$ describes the influence of tensile loading on the activation barrier, and

$C = \frac{32\pi\gamma\gamma_m^3}{3v_{f0}}$ is a coefficient associated with the influence of tensile loading on the number of subcritical nuclei.

D. Calculation result and discussion

To test the reliability of our void nucleation model, we choose Vit 1 from our spallation experiment as a model

material. The material parameters of Vit 1 are obtained from other works[21,33,44,45,51] and listed in Table III. Using the typical values $\Delta G^m = 0.35\ eV$, $n_0 = 6.14 \times 10^{22}\ \mathrm{cm}^{-3}$, $v^* \approx 20A^3$, $T = 300\ K$, and $v_{f0} \approx v^*/10 = 2A^3$, we can get the $\dot{N} \sim \sigma_T$ diagram by Eq. (18).

Figure 7 shows the nucleation rate function, Eq. (18), versus the applied tensile stress. In this diagram, the horizontal axis represents the applied tensile stress, and the logarithmic value of the nucleation rate is recorded on the vertical scale. The blue curve, plotted by Eq. (18) using material parameters of Vit 1, gives the variation of the nucleation rate with the applied tensile stress. If the value zero on the vertical scale is designated as the critical value below which void nucleation is so weak that it can be neglected, the resultant threshold stress of void nucleation for Vit. 1 is about 2.35 GPa (the black point in Fig. 7). This threshold stress is higher than the quasistatic tensile strength of Vit.1, 1.86 GPa.[51] As the spall strength is usually thought to be higher than the quasistatic tensile strength because of the loading rate effect, the threshold stress obtained by Eq. (18) is reasonable. This is favorable for our nucleation model.

We can also compare the calculated result with our experimental data. From the observed cellular pattern in Fig. 4(b), we determine the diameter of the microvoids to be about 2 μm. The duration of dynamic tensile stress is about 200 ns. Assuming that the microvoids are directly developed from nucleation and growth without coalescence, each cell in the cellular pattern could be seen as one microvoid corresponding to one nucleation site. Then, the average void nucleation rate can be estimated using

$$\bar{\dot{N}} = \frac{N}{t_n} \approx \frac{1}{d_v^3 \Delta t} = \frac{1}{(2\mu\mathrm{m})^3 \cdot 200\mathrm{ns}} = 6.25 \times 10^{17} \mathrm{cm}^{-3} s^{-1}, \tag{19}$$

where N is the number of nucleated microvoids per unit volume, t_n the time for nucleation, d_v the diameter of microvoids that is observed in the cellular pattern ($1/d_v^3$ is a rough estimate of the number of nucleated microvoids per unit volume), and Δt the duration of applied tensile stress used to estimate the time for nucleation.

Noting that the applied tensile stress is about 3.2 GPa in current spall experiments, the value obtained from Eq. (19) is marked with a white point in Fig. 7. As shown in Fig. 7, the value estimated from Eq. (19) is lower than that calculated by Eq. (18). This is expected. As void coalescence is ignored and the duration of a whole spallation is longer than the nucleation time, the real nucleation rate should be higher than the value of $\bar{\dot{N}}$ estimated by Eq. (19). Whereas, the theoretical nucleation rate obtained by Eq. (18) is also larger than the estimated one, the rate obtained by Eq. (18) is very likely close to the real one.

TABLE III. Material parameters of Vit 1.

Properties and parameters	Value	Material
Surface energy γ_m (J/m^2)	0.83	Vit 1
Average atomic volume Ω (A^3)	20	Vit 1
Migration volume V_m (Ω)	0.43	[a]$Ni_{50}Zr_{50}$
Geometry factor γ	0.105	Vit 1
Activation barrier ΔG^m (eV)	0.2–0.5	Vit 1

[a]The migration volume of $Ni_{50}Zr_{50}$ is used as a rough estimate for that of Vit 1.

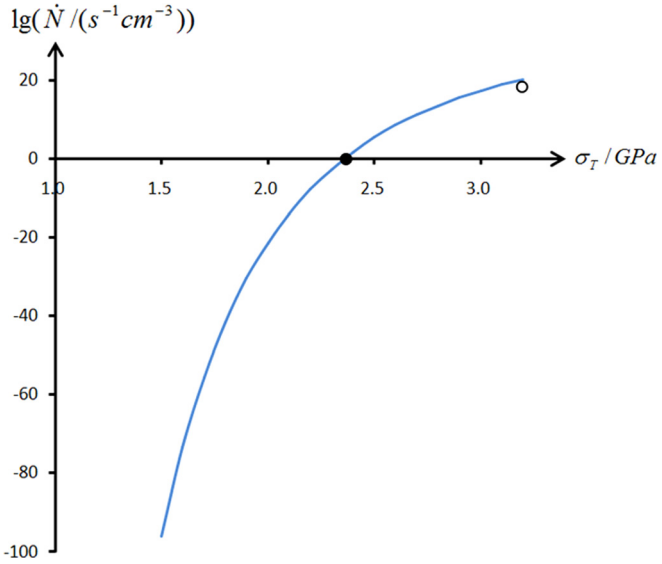

FIG. 7. (Color online) Void nucleation rate as a function of applied tensile stress.

V. CONCLUSION

A Zr-based amorphous alloy was subjected to dynamic tensile loading of identical amplitude ($\sim$3.18 GPa) but with different durations (83–201 ns) to reveal the micro-damage evolution process during spallation. Under the identical stress amplitude, samples with different durations show different levels of spallation damage: (1) no cracks, (2) a 200–250-μm crack which is partly parallel to the sample surface, and (3) a detached spallation. We carefully examined the spall surface and observed a cellular pattern with an equiaxed shape. It is revealed that (1) spallation in amorphous alloys is a kind of ductile fracture at the microscopic level; (2) spallation damages in amorphous alloys are microvoids; and (3) high mean tensile stress plays a dominant role during microvoid nucleation. To understand the mechanism of void nucleation in amorphous alloys, we proposed a void nucleation model based on free-volume theory. In this model, free volume and mean tensile stress play major roles in void nucleation. We proposed an explicit expression for the void nucleation rate, and the calculated results show our model to be reasonable. We believe that these findings are important to understand the mechanism of spallation in amorphous alloys.

ACKNOWLEDGMENTS

Financial support was from the NSFC (Grant Nos. 10872206, 10721202, 10725211, and 11132011), the National Natural Science Foundation of China-NSAF. Grant No: 10976100, and the National Basic Research Program of China (Grant No. 2009CB724401).

[1]D. R. Curran, L. Seaman, and D. A. Shockey, Phys. Rep. **147**, 253 (1987).
[2]M. A. Meyers, *Dynamic Behaviour of Materials* (Wiley, New York, 1994).
[3]R. J. Clifton, Int. J. Solids Struct. **37**, 105 (2000).
[4]A. Molinari and T. W. Wright, J. Mech. Phys. Solids **53**, 1476 (2005).
[5]D. N. Chen, C. L. Fan, S. G. Xie, J. W. Hu, S. X. Wu, H. R. Wang, H. Ta, and Y. Y. Yu, J. Appl. Phys. **101**, 014325 (2007).
[6]Y. L. Bai, Z. Ling, L. M. Luo, and F. J. Ke, Trans. ASME, J. Appl. Mech. **59**, 622 (1992).
[7]Y. L. Bai, J. Bai, H. L. Li, F. J. Ke, and M. F. Xia, Int. J. Impact Eng. **24**, 685 (2000).
[8]W. H. Wang, C. Dong, and C. H. Shek, Mater. Sci. Eng. R **44**, 45 (2004).
[9]M. M. Trexler and N. N. Thadhani, Prog. Mater Sci. **55**, 759 (2010).
[10]C. A. Schuh, T. C. Hufnagel, and U. Ramamurty, Acta Mater. **55**, 4067 (2007).
[11]W. Klement, R. H. Willens, and P. Duwez, Nature **187**, 869 (1960).
[12]W. L. Johnson, Prog. Mater Sci. **30**, 81 (1986).
[13]A. Inoue, A. Kato, T. Zhang, S. G. Kim, and T. Masumoto, Mater. Trans., JIM **32**, 609 (1991), available at http://www.jim.or.jp/journal/e/pdf3/32/07/609.pdf.
[14]A. Peker and W. L. Johnson, Appl. Phys. Lett. **63**, 2342 (1993).
[15]A. L. Greer, Science **267**, 1947 (1995).
[16]F. Spaepen, Acta Metall. **25**, 407 (1977).
[17]M. H. Cohen and G. S. Grest, Phys. Rev. B **20**, 1077 (1979).
[18]A. S. Argon, Acta Metall. **27**, 47 (1979).
[19]M. L. Falk and J. S. Langer, Phys. Rev. E **57**, 7192 (1998).
[20]D. Pan, A. Inoue, T. Sakurai, and M. W. Chen, Proc. Natl. Acad. Sci. U.S.A. **105**, 14769 (2008).
[21]M. Q. Jiang, Z. Ling, J. X. Meng, and L. H. Dai, Philos. Mag. **88**, 407 (2008).
[22]M. Q. Jiang, J. X. Meng, J. B. Gao, X. L. Wang, T. Rouxel, V. Keryvin, Z. Ling, and L. H. Dai, Intermetallics **18**, 2468 (2010).
[23]R. Raghavan, P. Murali, and U. Ramamurty, Acta Mater. **57**, 3332 (2009).
[24]J. P. Escobedo and Y. M. Gupta, J. Appl. Phys. **107**, 123502 (2010).
[25]S. M. Zhuang, J. Lu, and G. Ravichandran, Appl. Phys. Lett. **80**, 4522 (2002).
[26]S. J. Turneaure, S. K. Dwivedi, and Y. M. Gupta, J. Appl. Phys. **101**, 043514 (2007).
[27]F. P. Yuan, V. Prakash, and J. J. Lewandowski, J. Mater. Res. **22**, 402 (2007).
[28]F. P. Yuan, V. Prakash, and J. J. Lewandowski, Mech. Mater. **41**, 886 (2009).
[29]M. Martin, L. Kecskesb, and N. N. Thadhani, Scr. Mater. **59**, 688 (2008).
[30]M. Martin, L. Kecskes, N. N. Thadhani, in *Shock Compression of Condensed Matter - 2007, Pts 1 and 2*, edited by M. Elert, M. D. Furnish, R. Chau, N. C. Holmes, and J. Nguyen (Waikoloa, Hawaii, 2007), Vol. 955, p. 561.
[31]M. Martin, T. Sekine, T. Kobayashi, L. Kecskes, and N. N. Thadhani, Metall. Mater. Trans. A **38A**, 2689 (2007).
[32]J. X. Meng, Z. Ling, M. Q. Jiang, H. S. Zhang, and L. H. Dai, Appl. Phys. Lett. **92**, 171909 (2008).
[33]M. Q. Jiang and L. H. Dai, J. Mech. Phys. Solids **57**, 1267 (2009).
[34]K. M. Flores and R. H. Dauskardt, Acta Mater. **49**, 2527 (2001).
[35]J. M. Wilgeroth, P. J. Hazell, and G. J. Appleby-Thomas, J. Appl. Phys. **108**, 033524 (2010).
[36]J. M. Boteler and D. P. Dandekar, in *Shock Compression of Condensed Matter*, edited by M. Elert, M. D. Furnish, R. Chau, N. Holmes, and J. Nguyen (AIP, New York, 2007), p. 481.
[37]Z. Ling and L. T. Shen, J. Phys. IV **134**, 957 (2006).
[38]D. Hull and D. E. Rimmer, Philos. Mag. **4**, 673 (1959).
[39]R. Raj, Acta Metall. **26**, 995 (1978).
[40]R. Raj and M. F. Ashby, Acta Metall. **23**, 653 (1975).
[41]U. Geyer, S. Schneider, W. L. Johnson, Y. Qiu, T. A. Tombrello, and M. P. Macht, Phys. Rev. Lett. **75**, 2364 (1995).
[42]D. Turnbull and M. H. Cohen, J. Chem. Phys. **34**, 120 (1961).
[43]M. H. Cohen and D. Turnbull, J. Chem. Phys **31**, 1164 (1959).
[44]F. Faupel, W. Frank, M. P. Macht, H. Mehrer, V. Naundorf, K. Ratzke, H. R. Schober, S. K. Sharma, and H. Teichler, Rev. Mod. Phys. **75**, 237 (2003).
[45]Q. Yang, A. Mota, and M. Ortiz, Comput. Mech. **37**, 194 (2006).
[46]J. C. Dyre, Phys. Rev. B **75**, 092102 (2007).
[47]M. Q. Jiang and L. H. Dai, Phys. Rev. B **76**, 054204 (2007).
[48]B. Arman, S.-N. Luo, T. C. Germann, and T. Çağın, Phys. Rev. B **81**, 144201 (2010).
[49]A. C. Lund and C. A. Schuh, Acta Mater. **51**, 5399 (2003).
[50]P. G. Shewmon, *Diffusion in Solids*, 2nd ed. (The Minerals, Metals & Materials Society, United States, 1989).
[51]J. Lu, G. Ravichandran, and W. L. Johnson, Acta Mater. **51**, 3429 (2003).